

# Valley Bosonic Stimulation of Exciton-Polaritons in a Monolayer Semiconductor

Pasquale Cilibrizzi<sup>1</sup>, Xiaoze Liu<sup>1</sup>, Peiyao Zhang<sup>1</sup>, Chenzhe Wang<sup>1</sup>, Sui Yang<sup>1</sup>, Xiang Zhang<sup>1</sup>

<sup>1</sup> NSF Nanoscale Science and Engineering Center, University of California, Berkeley, California 94720, USA

**Abstract.** The newly discovered valley degree of freedom (DOF) in atomically thin two-dimensional (2D) transition metal dichalcogenides (TMDs) offers a promising platform to explore rich nonlinear physics, such as spinor Bose-Einstein condensate (BEC) and novel valleytronics applications. However, the critical nonlinear effect, such as valley polariton bosonic stimulation (BS), has long remained an unresolved challenge due to the generation of limited polariton ground state densities necessary to induce the stimulated scattering of polaritons in specific valleys. Here, we report, for the first time, the valley bosonic stimulation of exciton-polaritons via spin-valley locking in a WS<sub>2</sub> monolayer microcavity. This is achieved by the resonant injection of valley polaritons at specific energy and wavevector, which allows spin-polarized polaritons to efficiently populate their ground state and induce a valley-dependent bosonic stimulation. As a result, we observe the nonlinear self-amplification of polariton emission from the valley-dependent ground state. Our finding paves the way for both fundamental study of valley polariton BEC physics and non-linear optoelectronic devices such as spin-dependent parametric oscillators and spin-lasers.

The optical properties of a semiconductor are intrinsically related to its electronic band structure. The broken inversion symmetry in recently emerging two-dimensional (2D) transition metal dichalcogenides (TMDs) leads to two energy degenerate valleys at two corners of the first Brillouin zone, referred as K and K' valleys [1, 2]. Strong spin-orbit coupling locks the valley degree of freedom (DOF) to the electron and hole spins, resulting in specific optical selection rules of excitons [3]. Specifically, excitons in K and K' valleys can be selectively addressed using  $\sigma_+$  and  $\sigma_-$  circularly polarized optical excitations. These intriguing properties and the possibility to control valley DOF open new ways to explore spinor/valleytronic physics and novel optoelectronic applications [4].

Exciton-polaritons (hereafter polaritons), resulting from the strong coupling of cavity photons with TMD excitons [5], are composite bosonic quasi-particles, which can also be optically initialized in specific valleys [6-10]. In particular, polaritons in TMDs monolayer benefit from cavity protection effects, enhancing the valley polarization of excitons in TMD materials [7, 8], and diffusion lengths

longer than excitons in a bare monolayer [11,12], allowing for spin- and valley- selective propagation through the valley optical spin hall effect [13]. Non-resonant experiments have been studied in which the generation of polaritons is mediated by the population of an exciton reservoir. Yet it usually suffers from, for example, the reduced PL emission, due to exciton-exciton annihilation processes [14, 15] and additional valley depolarization effects, induced by exciton-exciton Coulomb exchange interactions [16, 17]. A critical step to advance TMD polaritons, as a practical platform to manipulate valley DOF in polariton Bose-Einstein condensates (BECs) [18] and exploit the valley polariton-polariton interactions for novel valleytronics applications, is the realization of the polariton nonlinear amplification, known as bosonic stimulation (BS), in specific valleys. However, valley BS has remained a major challenge so far, due to the significant difficulties in generating the polariton ground state densities necessary to induce the stimulated scattering of polaritons in desired valleys [19].

Here, we demonstrate the first valley bosonic stimulation in a WS<sub>2</sub> monolayer microcavity. We observe the nonlinear increase of the polariton emission co-polarized with the pump, a key signature of the valley bosonic stimulation. This process is facilitated by the spin-valley locking mechanism inherited by TMD polaritons from their exciton components, allowing polaritons to efficiently retain their valley polarization during their energy and momentum relaxation. Our findings show that polaritons can undergo a self-induced valley-dependent bosonic stimulation, which is the first step toward the realization of spinor polariton BEC and related topological effects in 2D TMD monolayers, as well as nonlinear valleytronic devices, such as spin switches, optical circuits based on polariton neurons and spin lasers, opening up new possibilities to merge valleytronics to the many-body physics of polaritons.

We resonantly inject exciton-polaritons at specific energy and wavevector ( $k$ ) and with specific spin orientation. Since polaritons are coherently injected in the microcavity, we do not create an exciton reservoir, thus limiting the density-dependent excitonic effects responsible for the reduction of valley polarization in TMD monolayers [16]. The spin-valley locking behaviour inherited from TMD excitons (Fig.1a), persists onto the hybrid polariton state, thus ensuring the generation of a ground state polariton population, co-polarized with the pump (e.g., spin-down,  $\sigma^-$  in Fig.1b). Since the energy and momentum-relaxation of polaritons are spin-dependent [20, 21], spin-down (-up) ground state polaritons stimulate the scattering of other high-energy spin-down (-up) polaritons (Fig.1b). Thus, upon increasing the polariton density, the valley bosonic stimulated scattering leads to the nonlinear amplification of the PL intensity and a high-degree (i.e., 64 %) of valley polarization in momentum space.

The microcavity (MC) sample consists of a single monolayer WS<sub>2</sub> embedded between two distributed Bragg reflectors (DBRs) as illustrated in Fig.2a (see the Methods section for details). In the experiments, the sample was held in a cold finger cryostat at a temperature of 80 K (schematically shown in the SI). A mode-locked Ti-sapphire pulsed laser (200 fs, 80 MHz) with 40.7 meV full width at half maximum (FWHM), is spectrally filtered to obtain pump pulses of 4.1 meV FWHM, as shown in Fig.2b (red profile). The excitation beam is circularly polarized (i.e.,  $\sigma_+$  or  $\sigma_-$ ) and focused to a 1.7  $\mu\text{m}$  FWHM spot diameter using a 0.60 numerical aperture microscope objective. PL from the LP branch at  $k \sim 0$ , is collected in reflection geometry through the excitation microscope objective (ensuring a  $\pm 37^\circ$  collection angle), analysed by a polarimeter composed of a  $\lambda/4$  and  $\lambda/2$  plates plus a linear polarizer and projected on the entrance slit of a spectrometer (see SI for details). To excite the MC with a specific angle, the excitation beam enters the focusing objective off-centre. We select the specific excitation angle by imaging simultaneously the pump laser and the PL emission, as shown in section S2 of the SI. The angle ( $\theta_p$ ) and energy ( $E_p$ ) of excitation used in the experiments, have been estimated from the conservation of the energy and momentum, as required by the scattering relaxation mechanism of polaritons, under resonant excitation [21] (see SI, section S3 for details).

Experimentally, the bosonic stimulation regime can be probed by driving the system resonantly with the laser and performing energy and wavevector resolved-spectroscopy (Fig. 2b). Specifically, we excite the sample at  $E_p = 2.0557$  eV and  $\theta_p = 11^\circ$  angle. These excitation parameters allow us to resonantly generate polaritons at  $k_p = 1.9 \mu\text{m}^{-1}$  close to the inflection point of the LP dispersion. To filter out the excitation laser, we spectrally filter the emission from the MC sample, as indicated by the green dotted line in Fig.2b, and detect the PL polariton emission from the lowest energy state of the LP dispersion. Polaritons injected at  $k_p$  and  $E_p$ , relax down to their ground state, populate the bottom of the LP dispersion at  $k \sim 0$  and leak out through the top cavity DBR mirror [22]. By repeating the reciprocal space spectroscopic imaging under non-resonant optical excitation (i.e., at  $E = 2.214$  eV, as described in the SI, section S4), we can collect the whole LP polariton dispersion (Fig.S4b of SI) and confirm that the PL emission we detect in our resonant experiments (Fig. 2b) corresponds to polaritons that accumulate in the lowest energy state (at  $k \sim 0$ ) of the LP dispersion (see SI, section S4 for details).

To demonstrate the valley bosonic stimulation of polaritons into the lowest LP energy states at  $k \sim 0$ , circularly polarized power dependence measurements are performed with selected excitation of  $\sigma_+$  ( $\sigma_-$ ) polarized polaritons in both K and K' valleys. By increasing the circularly polarized ( $\sigma_+$ ) excitation fluence, we increase the polariton density and observe a nonlinear increase of the co-polarized polaritons, as shown in Fig.3a (red circles,  $\sigma_+$ ). When we excite the MC with the opposite

circular polarization ( $\sigma^-$ ), we confirm the same nonlinear behaviour for the co-polarized polaritons generated in the K' valley, as shown in Fig.3b (blue circles,  $\sigma^-$ ). The nonlinear increase of the polariton emission from the lowest energy states is a clear signature of the bosonic final-state stimulation, which is a quantum statistical property of all bosons and the driving mechanism behind matter-wave amplification of both atomic [23] and polariton [18] BEC. The scattering rate of bosons into a certain quantum state is proportional to the number of bosons already occupying that state. In particular, the presence of N bosons in the final state, enhances the scattering rate of other bosons by a factor  $1 + N$ , thus effectively accelerating the energy relaxation process and stimulating the scattering of other identical bosons in the same state [22]. Therefore, with increasing polariton density, the co-polarized polariton relaxation rate increases, eventually overcoming the threshold for bosonic stimulation, when the relaxation into the ground state of the LP overcome its radiative decay, resulting in a super-linear increase of the polariton density at the bottom of the LP dispersion in both K (Fig.3a, red circles) and K' (Fig.3b, blue circles) valleys. The different threshold that we observe may be due to fluctuations in substrate adhesion, defects, strain and surface charge density [24-27]. The amplification ratio in both K and K' valleys, estimated as the intensity ratio of the polariton emission before and after threshold, is  $\sim 7$  (see SI, Fig. S6 for details).

On the other hand, the cross-circular polarized PL intensities, corresponding to polaritons scattering in the opposite valley respect to the one where they were initially generated, show only a linear increase with increasing fluence. This confirms that, by resonantly injecting polaritons in the LP dispersion at specific energy and wavevector (eq. 3 and eq. 4 in SI, section S3), we can generate the polariton density necessary to induce the bosonic stimulation of polaritons in the same valley, thus facilitating the intra-valley scattering of polaritons to overcome the inter-valley scattering, typical of WS<sub>2</sub> excitons [28]. Moreover, in our experiments, no injection of an initial population of polaritons at  $k \sim 0$  is required to stimulate the scattering of polaritons in the lowest energy state, like for example in pump-probe experiments [19]. We observe a self-induced valley bosonic stimulation, confirming that our excitation parameters ( $k_p$ ,  $E_p$ ) allow, in each valley, the generation of a density of polaritons sufficient to overcome the stimulation threshold.

Finally, the spin-valley locking mechanism is uniquely probed by the generation of valley polaritons and the conservation of their spin in each valley (Fig. 4a and Fig. 4b). To investigate the spin conservation of polaritons associated with their valley polarization, we calculate the circular degree of polarization (CDP) from the polarization resolved k-space spectroscopy images acquired during the power dependence measurements. As expected from the optical selection rules, a  $\sigma^+$  ( $\sigma^-$ ) circularly polarized excitation beam, will generate co-polarized polaritons in K (K') valley in momentum space, resulting in opposite sign of the CDP of polariton emission, as shown in Fig.4a

and Fig.4b. In other words, resonantly injected polaritons in K (K') valley highly retain the  $\sigma^+$  ( $\sigma^-$ ) circular polarization of the pump during their energy and momentum relaxation. The non-unitary circular degree of polarization that we observe is due to depolarization mechanisms. Many experimental studies [17, 28] have shown that the spin relaxation dynamics in TMDs is dominated by the presence of at least two main depolarization mechanisms: (1) the Maialle-Silve-Sham (MSS) mechanism [29], which is induced by the longitudinal-transverse (LT) splitting of the exciton energy and, ultimately, by the long range Coulomb exchange interaction between the electrons and holes composing the excitons [30, 31]; (2) the intervalley scattering, due to both the long- and short-range exchange interactions [31] and the scattering by acoustic phonons [32, 33]. In addition, in tungsten-based materials the depolarization processes are more pronounced than in other TMD materials, due to the strong atomic spin-orbit coupling in the d-orbitals of the W atom, which induces a larger splitting of the valence band in both K and K' valleys and activate extra depolarization channels, such as the  $\Gamma$ -valley assisted intervalley scattering [28]. Thus, only a maximum valley polarization of  $\sim 35\%$  has been reported in  $\text{WS}_2$  monolayers at both cryogenic (i.e.,  $< 90$  K) [34] and room temperature [34, 35]. The combination of spin-valley locking mechanism of TMD materials and the faster energy relaxation dynamics induced by the valley bosonic stimulation, allow us to observe a degree of valley polarization of 64% for K-valley (53% for K'-valley polaritons) in  $\text{WS}_2$  monolayers, which usually displays low degree of valley polarization as bare monolayer [34, 35].

In summary, we have first demonstrated the valley bosonic stimulation of exciton-polaritons in a 2D TMD semiconductor. By coherently injecting polaritons at specific energy and k-vector of the LP dispersion, we overcome the challenges of generating sufficient polariton densities necessary to explore nonlinear optical processes in a TMD monolayer microcavity. More importantly, the subsequent valley polariton stimulated scattering leads to the unique spin-valley locking nonlinear amplification of the polariton emission. The exploration of spin-valley locking mechanism in exciton-polariton microcavities offers new possibilities for harnessing spin-dependent polariton-polariton interactions through the valley DOF, opening up new routes to explore spin and valley physics in cavity electrodynamics. The valley-dependent bosonic stimulation paves the way for the realization of spinor polariton BEC in TMD and novel many-body phenomena associated with the valley DOF, as well as low-threshold spin polarized lasers and nonlinear spin-locking valleytronic devices.

## Methods

### Microcavity fabrication

The microcavity (MC) sample consists of a single monolayer  $\text{WS}_2$  embedded between two distributed Bragg reflectors (DBRs), grown on top of a Si substrate, as schematically shown in Fig.2a. The bottom DBR consists of 12.5 pairs of  $\text{Nb}_2\text{O}_5/\text{SiO}_2$ , while the top DBR is composed by 6.5 of the same pairs. The monolayers  $\text{WS}_2$  flake (HQ Graphene, Inc.) is obtained via mechanical exfoliation and encapsulated between two layers of hydrogen silsesquioxane (HSQ), with the double purpose of protecting the  $\text{WS}_2$  flake during the fabrication process and preserving its optical and electronic properties. An additional layer of  $\text{Al}_2\text{O}_3$  is deposited on top of the HSQ, to further protect the  $\text{WS}_2$  flake from the high temperature plasma during the growth of the top DBR. By controlling the thickness of both HSQ layers, we design the MC to operate at cavity-exciton detuning  $\Delta = E_{\text{ph}} - E_{\text{ex}} = -14$  meV. In section S1 of the SI, we report the white light reflectivity measurements of the planar MC, which allow us to measure the photonic dispersion and extract the main parameters of the photonic cavity.

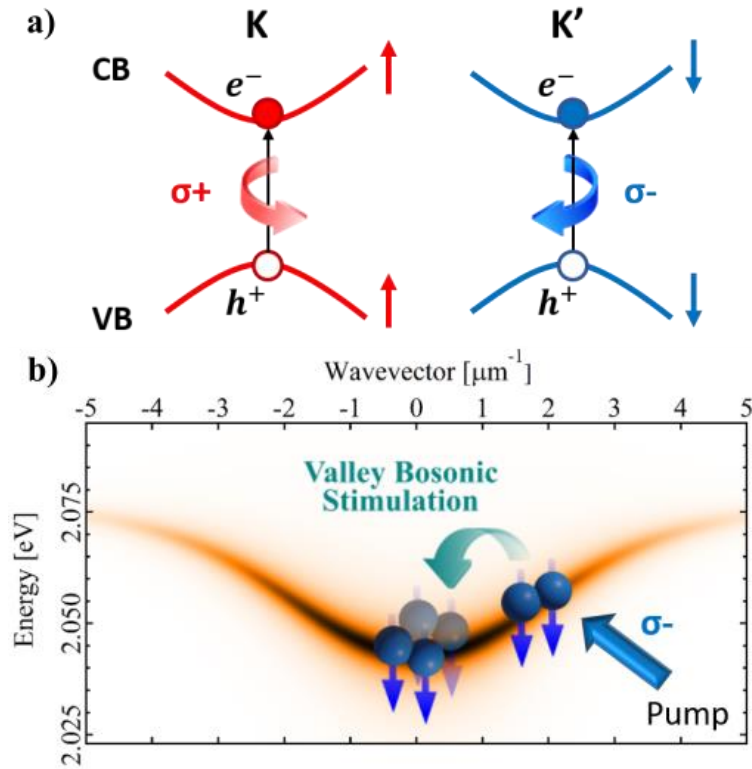


**Figure 1 - Schematic representation of the spin-valley locking mechanism and exciton-polariton valley bosonic final state stimulation.** (a) Two degenerate valleys, referred as K and K' valleys, are formed in WS<sub>2</sub> monolayer due to the absence of crystal inversion symmetry. Moreover, strong spin-orbits coupling further locks the valley index (K and K') to the electron (e<sup>-</sup>) and hole (h<sup>+</sup>) spins (up and down arrows), resulting in specific optical selection rules of excitons. In particular, excitons with opposite spins (i.e., +1 or -1) can be created in different valleys in momentum space (i.e., K and K'), by means of opposite circular polarized optical excitations (i.e.,  $\sigma^+$  or  $\sigma^-$ ) and can be optically detected, since their photoluminescence follows the same helicity of the excitation. (b) Schematic diagram of the valley bosonic stimulation induced by the resonant excitation scheme (blue arrow, “Pump”) used in the experiments (see SI, section S2 for details). Polaritons (blue spheres) resonantly injected in the lower polariton branch, with a spin set by the polarization of the pump ( $\sigma^-$ ), scatter toward the lower polariton energy state at  $k = 0$  (for illustrative purposes here we show only  $\sigma^-$  excitation). The presence of  $\sigma^-$  polaritons at  $k=0$ , stimulates the scattering of other polaritons with parallel spins, giving rise to a self-amplification of polariton emission from the valley-dependent ground state (i.e., valley bosonic stimulation).

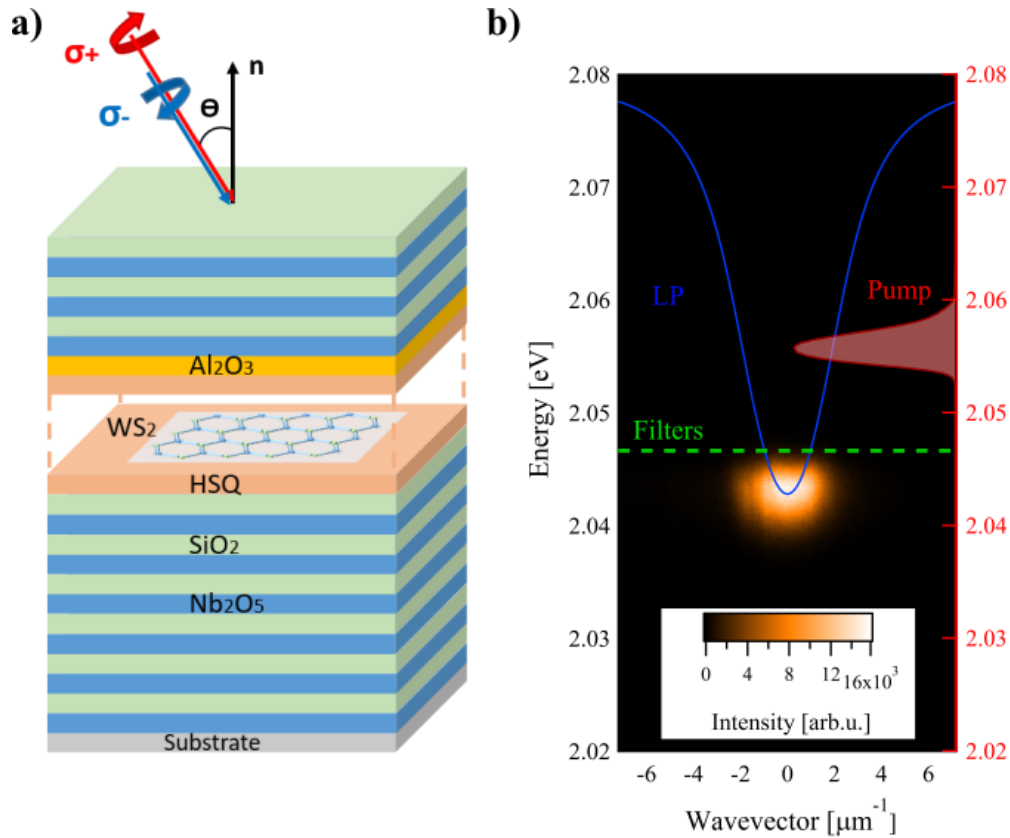


**Figure 2 - WS<sub>2</sub> polariton microcavity and resonant excitation scheme.** (a) The monolithic microcavity sample is composed by two Nb<sub>2</sub>O<sub>5</sub>/SiO<sub>2</sub> DBRs. The embedded WS<sub>2</sub> monolayer is sandwiched between two protective layers of HSQ and one layer of Al<sub>2</sub>O<sub>3</sub> (see Methods for details). The microcavity is excited with a  $\sigma_+$  ( $\sigma_-$ ) polarized beam set at an angle of incidence ( $\Theta$ ) relative to the microcavity's normal axis ( $n$ ). (b) Experimental energy and wavevector resolved emission intensity measured under resonant excitation ( $\sigma_+$  excitation,  $\sigma_+$  detection, pump fluence  $P = 137 \mu\text{J}/\text{cm}^2$ ). The red trace corresponds to the pump laser intensity profile used in the experiment. Polaritons injected resonantly with the lower polariton branch (“LP”, blue line), relax down to their ground state, populate the bottom of the LP dispersion at  $k \sim 0$  and leak out through the top cavity DBR mirror. To filter out the excitation laser (“Pump”, red trace), we spectrally filter the emission from the MC sample, as indicated by the green dotted line (see also Supplementary Information), and detect the PL polariton emission from the ground state of the LP dispersion at  $k=0$ .

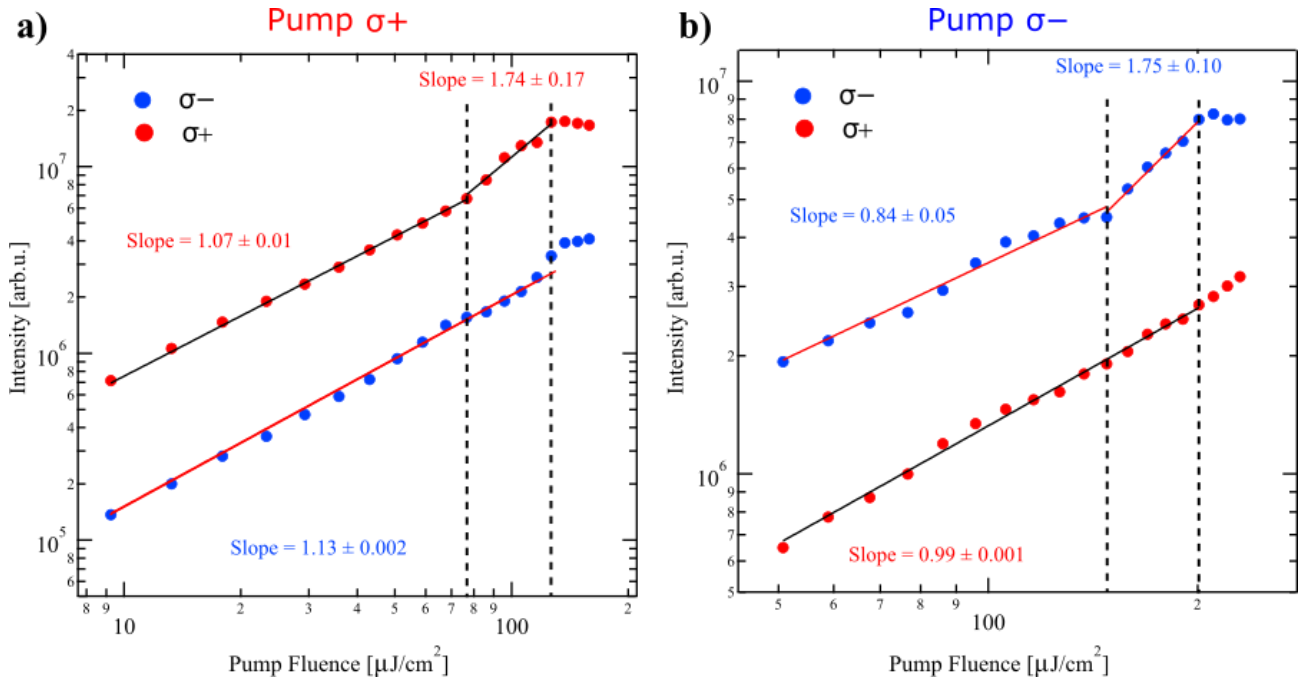


**Figure 3 - Self-amplification of the polariton emission at  $k = 0$  in both  $K$  and  $K'$  valleys.** The valley bosonic stimulation of polaritons into the lowest energy states at  $k \sim 0$ , is demonstrated by performing power dependence measurements. The sample is excited with  $\sigma_+$  ( $\sigma_-$ ) polarized pump, to generate polaritons in the  $K$  ( $K'$ ) valley and detect both co- and cross-circular polarization of the polariton emission, corresponding respectively to polaritons with the same and opposite polarization of the excitation pump. **(a)** The nonlinear increase of the polariton PL intensity co-polarized with the  $\sigma_+$  excitation pump (red circles), showing that polaritons excited in the  $K$ -valley undergo a nonlinear amplification. In contrast, the cross-polarized PL intensity (blue circles,  $\sigma_-$ ) exhibits only a linear increase with increasing fluence, as it corresponds to the intervalley scattering of polaritons from  $K$  to  $K'$  valley. **(b)** The nonlinear increase of the polariton PL intensity co-polarized with the  $\sigma_-$  excitation pump, confirming the valley bosonic stimulation also in the  $K'$  valley (blue circles). Also in this case, the cross-polarized PL intensity (red circles,  $\sigma_+$ ) exhibits a linear increase. The data are plotted in a log-log scale and fit with a power law of the form  $y(x) = kx^n$ , where  $n$  represents the slope of the lines used in the fittings. To record the evolution of the emission intensity with increasing excitation fluence, we integrate the LP emission (e.g., Fig. 2b), from 2.039 eV to 2.046 eV and  $|k| < 2.1 \mu\text{m}^{-1}$ . The vertical dotted lines highlight the nonlinear emission regime.

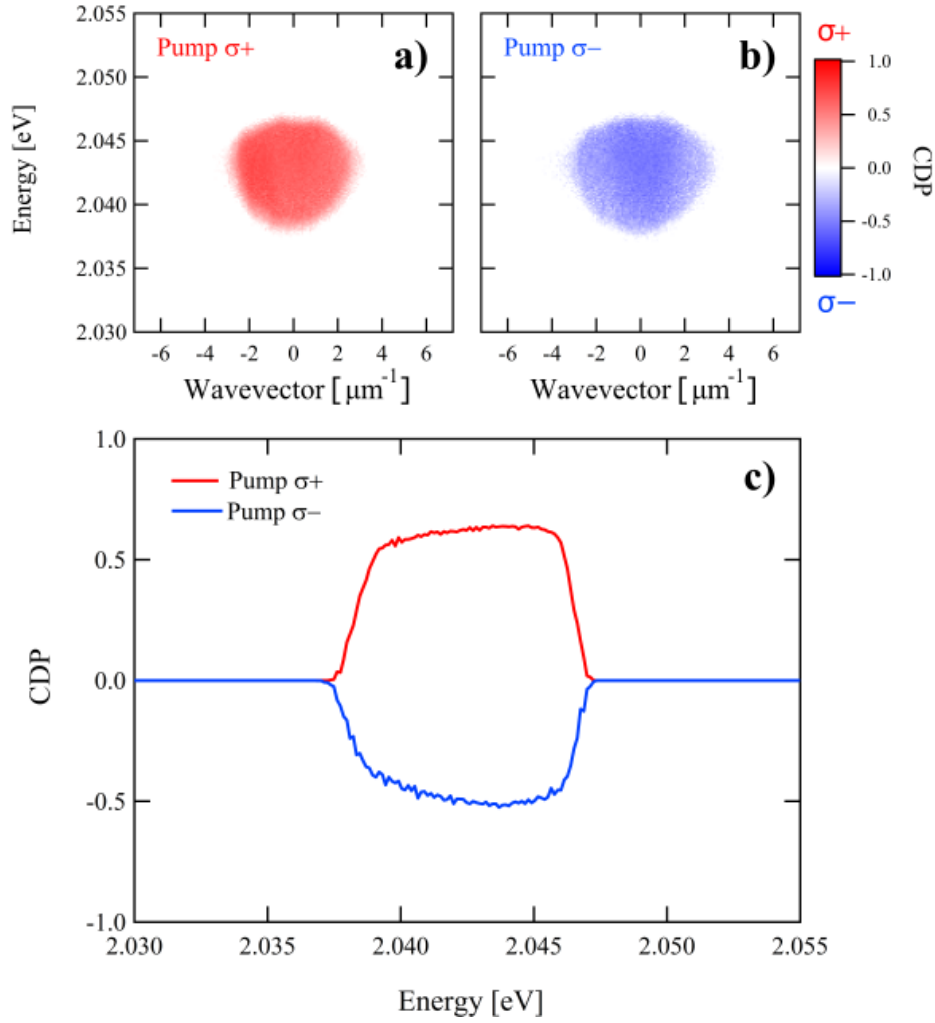


**Figure 4 - Ground-State ( $k = 0$ ) Polariton Valley-Polarized Emission in both K and K' valleys above the bosonic stimulation threshold.** The Circular Degree of Polarization (CDP) of the K-valley ground state polariton emission in momentum space, showing that polaritons co-polarized with the pump ( $\sigma_+$ ), scatter toward the lower polariton energy state at  $k = 0$ . Above the bosonic stimulation threshold, the bottom of the lower polariton dispersion, is uniformly populated by  $\sigma_+$  polaritons. **(b)** The CDP of the ground state polariton emission, confirming the uniform occupation of the lowest energy state by polaritons co-polarized with the pump ( $\sigma_-$ ) in K'-valley. The  $\sigma_+$  ( $\sigma_-$ ) circular polarization of the pump is largely preserved by K (K') valley polaritons, resulting in a positive (negative) sign of CDP in each valley represented, respectively, in red (blue) in the colorscale. Here,  $CDP = (I_{\sigma_+} - I_{\sigma_-}) / (I_{\sigma_+} + I_{\sigma_-})$ , with  $I_{\sigma_+}$  and  $I_{\sigma_-}$  being respectively the measured intensities of the two circular polarization components. **(c)** Horizontal profiles extracted at  $|k| < 1 \mu\text{m}^{-1}$  from (a), red profile, and (b) blue profile.

## Supplementary Information for

# Valley Bosonic Stimulation of Exciton-Polaritons in a Monolayer Semiconductor

Pasquale Cilibrizzi<sup>1</sup>, Xiaoze Liu<sup>1</sup>, Peiyao Zhang<sup>1</sup>, Chenzhe Wang<sup>1</sup>, Sui Yang<sup>1</sup>, Xiang Zhang<sup>1</sup>

<sup>1</sup> NSF Nanoscale Science and Engineering Center, University of California, Berkeley, California 94720, USA

### S1. CHARACTERIZATION OF THE PHOTONIC MICROCAVITY

In this section we report the white light reflectivity measurements of the MC sample used in the experiment. To measure the photonic dispersion, we excite an area of the sample away from the WS<sub>2</sub> monolayer and project the Fourier space of the microcavity in the entrance slit of the spectrometer (Fig. S2a).

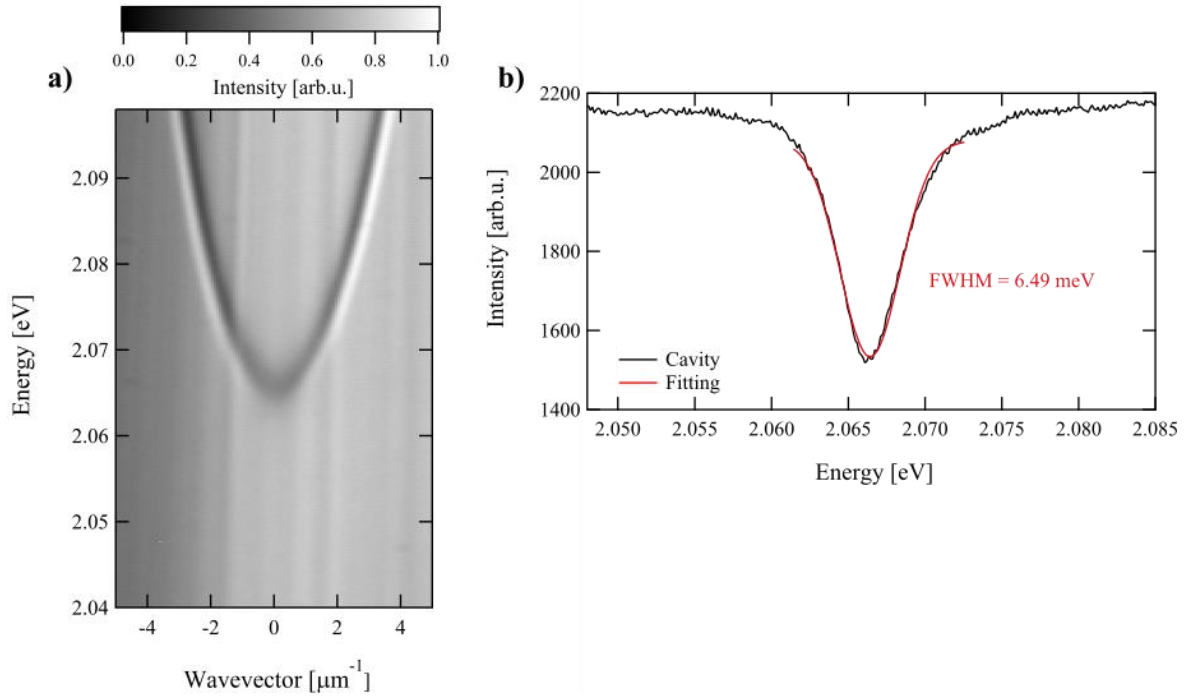


**Figure S2.** **a)** Experimental white light reflectivity measurements of the MC sample used in the experiment. **b)** Intensity profile extracted along the vertical axis in a), from 2.048eV to 2.085eV and  $|k| < 0.5\mu\text{m}^{-1}$ . The red line represents the inverse Gaussian fitting used to calculate the FWHM and the resonance of the photonic mode of the microcavity.

The main parameters of the photonic MC, extracted from the inverse Gaussian fitting (red line in Fig. S2b) of the bare cavity mode are reported below:

- Bare Cavity Resonance = 2.0664 eV

- Bare Cavity FWHM = 6.49 meV
- Q-factor = 318

## S2. EXCITATION ANGLE

In this section we report the energy–angle map of the microcavity under resonant excitation. By removing one filter in the detection path, we can collect both the PL and the pump (Figure S3) and confirm the excitation angle in our experiment.

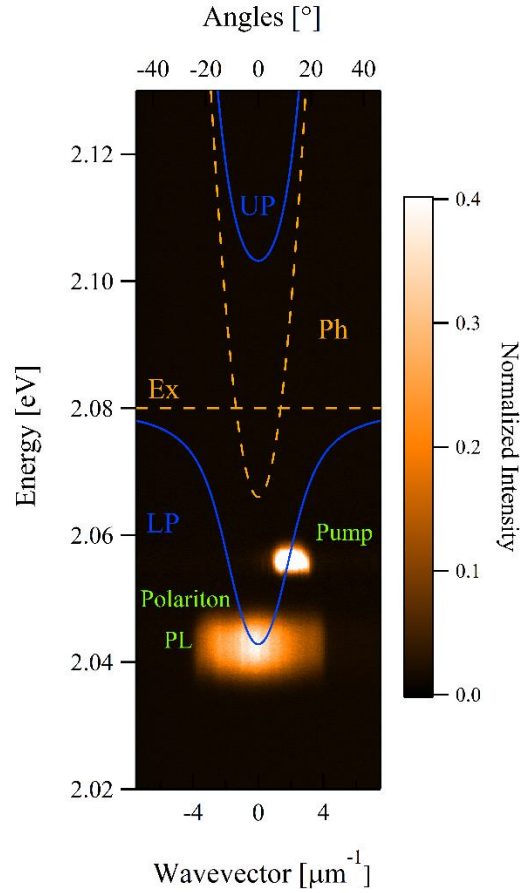


**Figure S3.** Energy and wavevector resolved emission intensity under resonant excitation, showing both the pump laser (“Pump”), which is incident at an angle  $\theta_p = 11^\circ$ , and the exciton-polariton photoluminescence (PL) emission. The intensity of the pump laser is saturated for illustrative purposes.

The incidence angle is related to the in-plane wavevector ( $k_{||}$ ) by means of the following relation:

$$k_{||} = \frac{2\pi}{\lambda_p} \sin \theta_p$$

where  $\lambda_p$  is the excitation wavelength and  $\theta_p$  is the incidence angle of the pump laser. The pump laser is in resonance with the lower polariton branch at an incidence angle of  $\vartheta_p = 11^\circ$ , with an angular full width at half maximum (FWHM) of  $\sim 10^\circ$  and at excitation energy of  $E_p = 2.557$  eV, with FWHM  $\sim 4$  meV.

### S3. ESTIMATION OF THE EXCITATION PARAMETERS

Under resonant excitation, the scattering process of polaritons requires the conservation of both energy and momentum [21]. In particular, two polaritons injected by the resonant pump, with energy and wavevector  $(E_p, k_p)$ , scatter into a lower  $(E_0, k_0)$  and higher  $(E_H, k_H)$  energy state, by conserving both energy and momentum. The latter condition requires that:

$$2 k_p = k_0 + k_H \quad (1)$$

$$2 E_p = E_0 + E_H \quad (2)$$

To estimate the energy and angle of excitation in our resonant experiments, we proceed as follows:

- we first measure the polariton dispersion under non resonant excitation (Fig. S4b), and extract the highest and lowest occupied energy states ( $E_H, E_0$  respectively) and their corresponding wavevector ( $k_0, k_H$ ) on the lower polariton dispersion (as indicated by the red crosses in Fig. S4b). The experimental values are:

$$E_0 = 2.0428 \text{ eV}, \quad k_0 = 0$$

$$E_H = 2.0686 \text{ eV}, \quad k_H = 3.8 \mu\text{m}^{-1}$$

- We then apply the conservation of momentum and energy, i.e., equations (1) and (2) above, to estimate the highest energy ( $E_p$ ) and wavevector ( $k_p$ ) of the excitation pump:

$$\text{From (1):} \quad k_p = \frac{k_0 + k_H}{2} = 1.9 \mu\text{m}^{-1} \quad (3)$$

$$\text{From (2):} \quad E_p = \frac{E_0 + E_H}{2} = 2.0557 \text{ eV} \quad (4)$$

The energy and wavevector above can then be converted in their corresponding values of wavelength and angle, by using the following relations (with  $h$  and  $c$  being respectively the Planck constant and the speed of light):

$$\lambda_p = \frac{h c}{E} = \frac{1240 \text{ eV} \cdot \text{nm}}{2.0557 \text{ eV}} = 603.2 \text{ nm} \quad (5)$$

$$\vartheta_p = \sin^{-1} \left( \frac{\lambda_p \cdot k_p}{2\pi} \right) = 10.5^\circ \quad (6)$$

which are the values that we use in our main experiment (Fig.3a and Fig3b of the main text).

In our experiments, the excitation laser is in resonance with the lower polariton branch at an incidence angle of  $\vartheta_p = 11^\circ$  and at excitation energy of  $E_p = 2.557 \text{ eV}$ . However, since the excitation beam covers a finite range of incidence angles ( $\sim 10^\circ$ ), larger than the polariton angular width ( $\sim 7^\circ$ ) at the value of energy corresponding to the energy of excitation ( $E_p$ ), the condition on the energy (eq. 2) is more critical than the condition on the angles or wavevector (eq. 1), as long as the excitation is in resonance with the lower polariton branch.

#### S4. POLARITON EMISSION: RESONANT VS NON RESONANT EXCITATION

In this section we report the momentum resolved spectroscopy of the MC sample under non-resonant excitation.

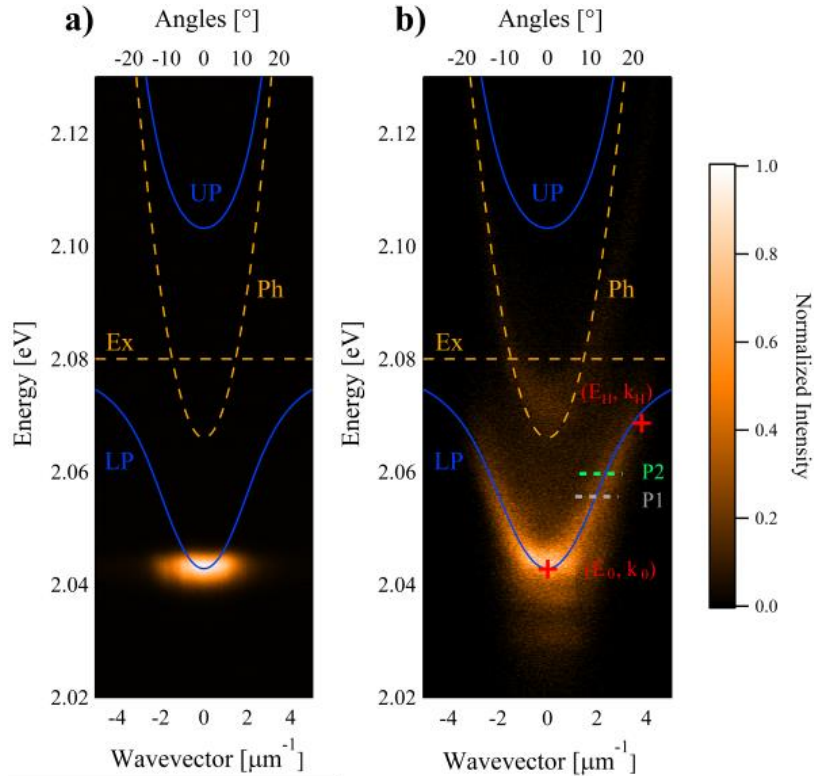


**Figure S4.** Energy and wavevector resolved emission intensity under, **a)** resonant and **b)** non resonant excitation. The yellow dotted lines represent the theoretical exciton (Ex) and photon (Ph) dispersion, while the blue lines represent the lower (LP) and upper (UP) polariton branches. The red crosses in b) represent the highest and lowest occupied energy values, that we use to estimate the angle and energy of excitation in section S3. P1 represents the energy of excitation used for the experiment described in the manuscript, while P2 corresponds to the control experiment presented in Section S5. The length of both P1 and P2 dotted lines, correspond to the angular aperture of the pump spot ( $\sim 10^\circ$ ).

The resonant excitation measurement (Fig. S4a) has been obtained with the experimental parameters reported in the main text, (i.e.,  $\vartheta_p = 11^\circ$ ,  $E_p = 2.557$  eV). The non-resonant excitation measurement (Fig. S4b) has been obtained by exciting the MC at the first reflectivity minimum above the cavity stop band, i.e., at  $E = 2.214$  eV in reflection geometry. The spectrally and in-plane wavevector ( $k$ ) resolved emission intensity is shown in Fig. S4b. By comparing the non-resonant dispersion (Fig. S4b) with the measurement performed under resonant excitation (Fig. S4a), we confirm that the PL emission we detect in our experiments, corresponds to polaritons that accumulate in the lowest energy state (at  $k \sim 0$ ) of the LP dispersion.

## S5. RESONANT EXPERIMENTS AT DIFFERENT EXCITATION ENERGY

In this section, we present circularly polarized ( $\sigma^+$ ) power dependence measurements performed at excitation angle  $\Theta_p = 11^\circ$  and energy  $E_p = 2.0598$  eV. These excitation parameters allow us to resonantly generate polaritons at higher excitation energy (position P2 in Fig. S4b) compared with  $E_p$  used to observe the valley bosonic stimulation (position P1 in Fig. S4b).

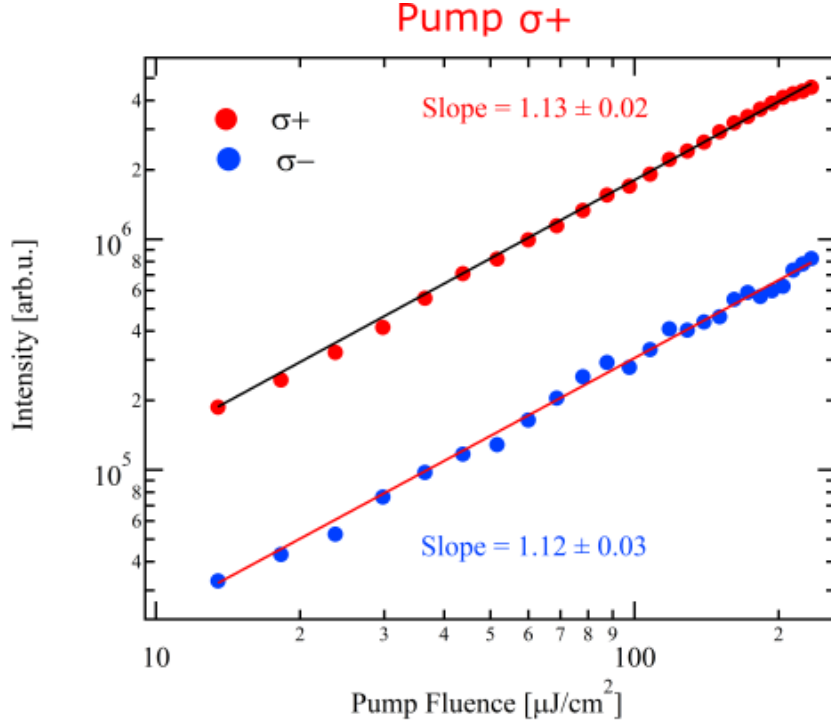


**Figure S5.** Power dependence measurements acquired under circular polarized ( $\sigma^+$ ) excitation with the same angle (i.e.,  $\Theta_p = 11^\circ$ ) as in Fig.3 of the main text, but with higher excitation energy ( $E_p = 2.0598$ eV), as shown by the dotted line P2 in Fig. S4b. The data are plotted in a log-log scale and fit with a power law of the form  $y(x) = kx^n$ , where  $n$  represents the slope of the lines used in the fittings.

We excite the MC with a  $\sigma^+$  polarized excitation beam and detect both the co- ( $\sigma^+$ ) and the cross-polarized ( $\sigma^-$ ) polariton emission, shown in Fig. S5 as red and blue trace, respectively. At higher excitation energy, we report a linearly increase of the polariton emission in both K and K' valley (Fig.S5), confirming that the condition on the energy (eq. 2 in Sec. S4) is critical to observe the valley bosonic stimulation.

## S6. AMPLIFICATION OF THE POLARITON EMISSION

In this section we report the PL spectra acquired with  $\sigma^+$  excitation/ $\sigma^+$  detection (Fig. S6a) and  $\sigma^-$  excitation/ $\sigma^-$  detection (Fig. S6b) at different excitation fluences, corresponding to polariton emission below (blue traces) and above (red traces) the bosonic stimulation threshold shown in Fig.3 of the main text. The amplification ratio, estimated as the intensity ratio of the polariton emission before and after threshold in both K (Fig. S6a) and K' valleys (Fig. S6b) is  $\sim 7$ .

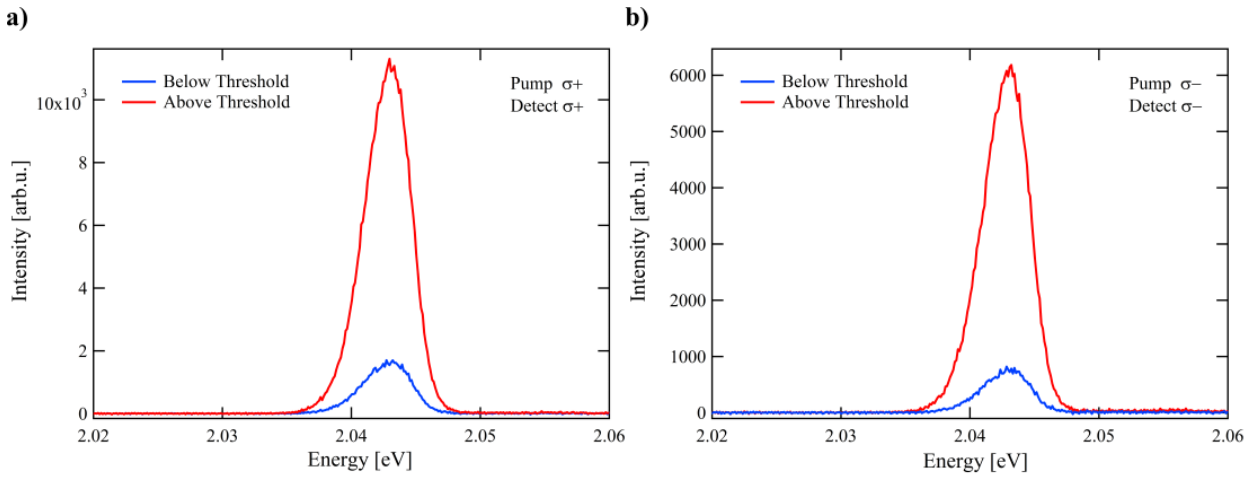


**Figure S6.** Energy resolved intensity profiles of the polariton emission, co-polarized with the excitation pump, in K (a) and K' (b) valley. The profiles have been extracted at excitation fluences below (blue trace) and above (red traces) the bosonic stimulation threshold.

## S7. EXPERIMENTAL SETUP

The microcavity (MC) sample consists of a single monolayer  $\text{WS}_2$  embedded between two distributed Bragg reflectors (DBRs) as illustrated in Fig.2a of the main text. The sample is held in a cold-finger cryostat at a temperature of 80K and is optically pumped at specific energy and wavevector, as indicated in the main text and in section S5. This excitation scheme allows us to resonantly pump the lower polariton (LP) dispersion. To excite the MC, a mode-locked Ti-sapphire pulsed laser (200 fs, 80 MHz) with 40.7 meV full width at half maximum (FWHM), is spectrally filtered by means of a combination of filters (“excitation filters” in Fig. S7) to obtain pump pulses of 4.1 meV FWHM, as shown in Fig.2b (red profile) of the main text. The excitation beam is circularly polarized (i.e.,  $\sigma^+$  or  $\sigma^-$ ) and focused to a  $1.7\mu\text{m}$  FWHM spot diameter using a 0.60 numerical aperture microscope objective. Photoluminescence (PL) from the LP branch at  $k\sim 0$ , is collected in reflection geometry through the excitation microscope objective (ensuring a  $\pm 37^\circ$  collection angle), analysed by a

polarimeter composed of  $\lambda/4$ ,  $\lambda/2$  plates and a linear polarizer (LP) and projected, by means of a lens system, on the entrance slit of a spectrometer.

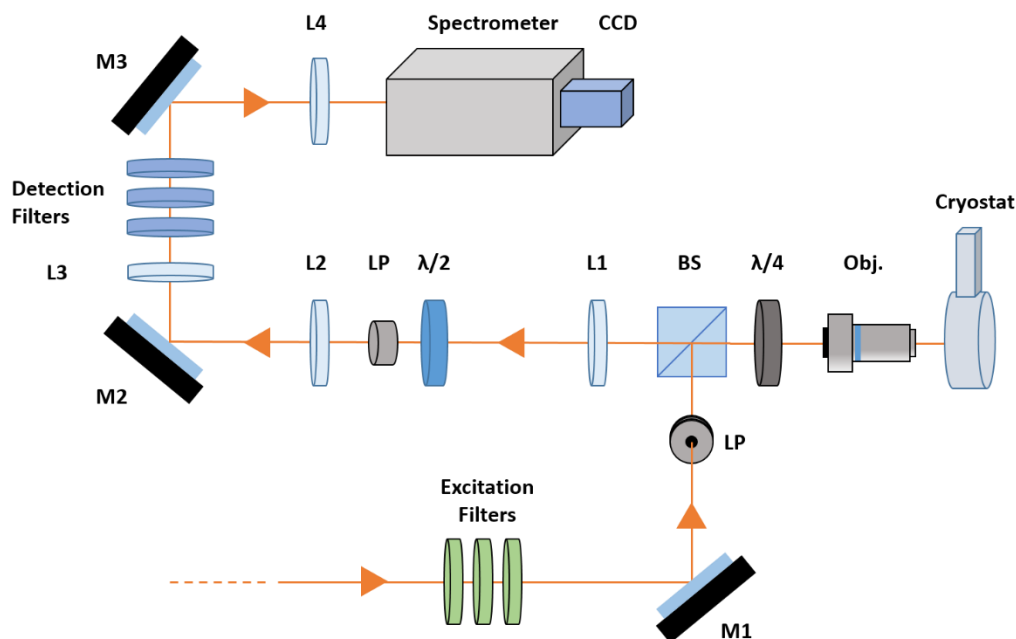


**Figure S7.** Sketch of the optical setup used in the experiments. List of the optical components: **M1**, **M2** and **M3** are mirrors; **LPs** are linear polarizers; **BS** is a non-polarizing beam splitters;  $\lambda/4$  is a quarter-wave plate; **Obj.** is the objective used for excitation and collection, with 40x magnification and 0.65 numerical aperture; **L1**, **L2**, **L3** and **L4** are convex lenses;  $\lambda/2$  and **LP** are respectively the quarter-wave plate and the linear polarizer used to measure the Stokes parameters.

The emission from the LP branch is then spectrally filtered by means of another combination of filters (“detection filters” in Fig. S7), to block out the excitation laser and collect only photons with energy  $\leq 2.049$  eV, which corresponds to the energy range of the bottom of the LP dispersion. To perform white-light reflection spectroscopy and characterize the MC sample (Fig. S2) we use a broadband (white) light source. A mirror on a flip mount and a second beam splitter was used for the white light to enter the same optical path of the laser. The reflected light is collected by the same objective and projected in the spectrometer by the same combination of lens used for the PL measurements.

## References

- [1] Xu, X., Yao, W., Xiao, D. et al. Spin and pseudospins in layered transition metal dichalcogenides. *Nature Phys.* **10**, 343–350 (2014).
- [2] Mak, K., Shan, J. Photonics and optoelectronics of 2D semiconductor transition metal dichalcogenides. *Nature Photon* **10**, 216–226 (2016).
- [3] Mak, K., He, K., Shan, J. et al. Control of valley polarization in monolayer MoS<sub>2</sub> by optical helicity. *Nature Nanotech* **7**, 494–498 (2012).
- [4] Schaibley, J., Yu, H., Clark, G. et al. Valleytronics in 2D materials. *Nat Rev Mater* **1**, 16055 (2016).
- [5] Schneider, C., Glazov, M.M., Korn, T. et al. Two-dimensional semiconductors in the regime of strong light-matter coupling. *Nat Commun* **9**, 2695 (2018).
- [6] Sun, Z., Gu, J., Ghazaryan, A. et al. Optical control of room-temperature valley polaritons. *Nature Photon* **11**, 491–496 (2017).
- [7] Chen, YJ., Cain, J., Stanev, T. et al. Valley-polarized exciton–polaritons in a monolayer semiconductor. *Nature Photon* **11**, 431–435 (2017).
- [8] Dufferwiel, S., Lyons, T., Solnyshkov, D. et al. Valley-addressable polaritons in atomically thin semiconductors. *Nature Photon* **11**, 497–501 (2017).
- [9] Grosso, G. Valley polaritons. *Nature Photon* **11**, 455–456 (2017).
- [10] M. Król, K. Lekenta, R. Mirek, et al. Valley polarization of exciton–polaritons in monolayer WSe<sub>2</sub> in a tunable microcavity. *Nanoscale* **11**, 9574 (2019).
- [11] Barachati, F., Fieramosca, A., Hafezian, S. et al. Interacting polariton fluids in a monolayer of tungsten disulfide. *Nature Nanotech* **13**, 906–909 (2018).
- [12] Kulig, M. et al. Exciton diffusion and halo effects in monolayer semiconductors. *Phys. Rev. Lett.* **120**, 207401 (2018).
- [13] Lundt, N., Dusanowski, Ł., Sedov, E. et al. Optical valley Hall effect for highly valley-coherent exciton-polaritons in an atomically thin semiconductor. *Nat. Nanotechnol.* **14**, 770–775 (2019).
- [14] Yu, Y. et al. Fundamental limits of exciton-exciton annihilation for light emission in transition metal dichalcogenide monolayers. *Phys. Rev. B* **93**, 201111 (2016).
- [15] Y. Lee, G. Ghimire, S. Roy et al. Impeding Exciton–Exciton Annihilation in Monolayer WS<sub>2</sub> by Laser Irradiation, *ACS Photonics* 2018, **5**, 7, 2904–291.
- [16] F. Mahmood, Z. Alpichshev, Y.-H. Lee, et al. Observation of Exciton–Exciton Interaction Mediated Valley Depolarization in Monolayer MoSe<sub>2</sub>. *Nano Lett.* 2018, **18**, 1, 223–228.
- [17] Lagarde, D. et al. Carrier and polarization dynamics in monolayer MoS<sub>2</sub>. *Phys. Rev. Lett.* **112**, 047401 (2014).

- [18] Kasprzak, J., Richard, M., Kundermann, S. et al. Bose–Einstein condensation of exciton polaritons. *Nature* **443**, 409–414 (2006).
- [19] Savvidis, P. G. et al. Angle-resonant stimulated polariton amplifier. *Phys. Rev. Lett.* **84**, 1547–1550 (2000).
- [20] I. A. Shelykh, A. V. Kavokin et al. Spin dynamics of exciton polaritons in microcavities. *Physica Status Solidi (b)* **242**, 2271 (2005).
- [21] A. Kavokin, J. J. Baumberg, et al. *Microcavities* (Oxford University Press, 2011).
- [22] Deng, H., Haug, H. & Yamamoto, Y. Exciton–polariton Bose–Einstein condensation. *Rev. Mod. Phys.* **82**, 1489–1537 (2010).
- [23] Miesner, H.-J. et al. Bosonic stimulation in the formation of a Bose-Einstein condensate. *Science* **279**, 1005–1007 (1998)
- [24] Y. Rong, Y. Fan, A. L. Koh, et al. Controlling sulphur precursor addition for large single crystal domains of WS<sub>2</sub>. *Nanoscale*, 2014, **6**, 12096 -12103 (2014).
- [25] Y. Kwon, K. Kim, W. Kim et al. Variation of photoluminescence spectral line shape of monolayer WS<sub>2</sub>. *Appl. Phys.* **18**, 941–945 (2018).
- [26] Zhu, B., Chen, X. & Cui, X. Exciton Binding Energy of Monolayer WS<sub>2</sub>. *Sci. Rep.* **5**, 9218 (2015).
- [27] Cong, C., Shang, J., Wang, Y. et al. Optical Properties of 2D Semiconductor WS<sub>2</sub>. *Adv. Opt. Mater.* **6**, 1700767 (2018).
- [28] Su, H., Deng, A., Zhen, Z. & Dai, J.-F.  $\Gamma$ -valley assisted intervalley scattering in monolayer and bilayer WS<sub>2</sub> revealed by time-resolved Kerr rotation spectroscopy. *Physical Review B* **97**, 115426 (2018).
- [29] Maialle, M. Z., de Andrada e Silva, E. A. & Sham, L. J. Exciton spin dynamics in quantum wells. *Phys. Rev. B* **47**, 15776–15788 (1993).
- [30] Glazov, M. M. et al. Exciton fine structure and spin decoherence in monolayers of transition metal dichalcogenides. *Phys. Rev. B* **89**, 201302 (2014).
- [31] Yu, T. & Wu, M. W. Valley depolarization due to intervalley and intravalley electron–hole exchange interactions in monolayer MoS<sub>2</sub>. *Phys. Rev. B* **89**, 205303 (2014).
- [32] Lu, H-Z., Yao, W., Xiao, D. & Shen, S-Q. Intervalley scattering and localization behaviors of spin–valley coupled Dirac fermions. *Phys. Rev. Lett.* **110**, 016806 (2013).
- [33] Carvalho, B., Wang, Y., Mignuzzi, S. et al. Intervalley scattering by acoustic phonons in two-dimensional MoS<sub>2</sub> revealed by double-resonance Raman spectroscopy. *Nat Commun* **8**, 14670 (2017).

- [34] Zhu, B., Zeng, H., Dai, J., Gong, Z. & Cui, X. Anomalously robust valley polarization and valley coherence in bilayer WS<sub>2</sub>. *Proc. Natl. Acad. Sci. U.S.A.* **111**, 11606–11611 (2014).
- [35] Nayak, P. K., Lin, F.-C., Yeh, C.-H., Huang, J.-S. & Chiu, P.-W. Robust room temperature valley polarization in monolayer and bilayer WS<sub>2</sub>. *Nanoscale* **8**, 6035–6042 (2016).